Journal of Advanced Ceramics
2022, **11**(3): 414–426
https://doi.org/10.1007/s40145-021-0544-4
ISSN 2226-4108
CN 10-1154/TQ

Research Article

Remarkably enhanced piezo-photocatalytic performance in $BaTiO_3$/CuO heterostructures for organic pollutant degradation

Chengye YU[a,b], Mengxi TAN[a,b], Chengdong TAO[a,b], Yuxuan HOU[a,b], Chuanbao LIU[c], Huimin MENG[b], Yanjing SU[a,b], Lijie QIAO[a,b], Yang BAI[a,b,*]

[a]*Beijing Advanced Innovation Center for Materials Genome Engineering, University of Science and Technology Beijing, Beijing 100083, China*
[b]*Institute for Advanced Material and Technology, University of Science and Technology Beijing, Beijing 100083, China*
[c]*School of Materials Science and Engineering, University of Science and Technology Beijing, Beijing 100083, China*

Received: August 20, 2021; Revised: October 1, 2021; Accepted: October 4, 2021

Abstract: Introducing polarization field of piezoelectric materials is an effective strategy to improve photocatalytic performance. In this study, a new type of $BaTiO_3$/CuO heterostructure catalyst was designed and synthesized to achieve high piezo-photocatalytic activity through the synergy of heterojunction and piezoelectric effect. The $BaTiO_3$/CuO heterostructure shows a significantly enhanced piezo-photocatalytic degradation efficiency of organic pollutants compared with the individual $BaTiO_3$ nanowires (NWs) and CuO nanoparticles (NPs). Under the co-excitation of ultrasonic vibration and ultraviolet radiation, the optimal degradation reaction rate constant k of polarized $BaTiO_3$/CuO heterostructure on methyl orange (MO) dye can reach 0.05 min^{-1}, which is 6.1 times of photocatalytic rate and 7 times of piezocatalytic rate. The $BaTiO_3$/CuO heterostructure with remarkable piezo-photocatalytic behavior provides a promising strategy for the development of high-efficiency catalysts for wastewater purification, and it also helps understand the coupling mechanism between piezoelectric effect and photocatalysis.

Keywords: piezotronics; photocatalysis; polarization; heterostructure

1 Introduction

The ever-increasing energy crisis and environmental pollution have seriously threatened the sustainable development of society [1–5]. As a promising technology to solve these problems, photocatalysis has attracted great interest. Semiconductor photocatalytic technology can directly convert solar energy into chemical energy, and realize the degradation of organic pollutants and water splitting, which is a "green" way to apply solar energy directly [6–8]. Nevertheless, one of the most serious problems hindering the practical application of semiconductor photocatalysts is the low catalytic efficiency due to the recombination of photo-generated electron–hole pairs [9–11]. To improve photocatalytic performance, it is important to accelerate the separation

* Corresponding author.
E-mail: baiy@mater.ustb.edu.cn

of photo-generated carriers both in the bulk and on the surface. To date, many strategies have been developed to overcome these limitations, such as ion doping, constructing heterostructure, co-catalyst loading, and nanostructure design [12–16]. Although the recombination of photo-generated carriers on the surface is suppressed by these methods, it is still hard to be eliminated in the bulk at present [17–19]. That is, the low photocatalytic activity is because only a small number of carriers reach the surface of photocatalyst to work for catalysis. Therefore, it is still a challenge to find an effective way to inhibit the recombination of photo-generated carriers.

Recently, it has attracted increasing attention to introduce the piezoelectric effect into the photocatalysis to improve catalytic activity [20–23]. In this process, a built-in electric field is established by piezoelectric effect to promote the separation of photo-generated electrons and holes. For example, Wang and Wu [24] reported a highly efficient hydrogen evolution reaction in ferroelectric *R*3*c* $LiNbO_3$-type $ZnSnO_3$ nanowires (NWs) through the piezo-phototronic effect because the mechanical force-induced spontaneous polarization drives photo-generated electrons and holes in opposite directions, thereby enhancing the redox process. Wang *et al.* [25] demonstrated that the organolead halide perovskite $CH_3NH_3PbI_3$ possesses markedly enhanced hydrogen generation under simultaneous ultrasonic and visible light illumination. Hu *et al.* [26] illustrated the enhanced oxygen reduction reaction performance of Bi_4NbO_8Br single-crystalline nanoplates owing to the piezo-phototronic effect. Furthermore, since the construction of semiconductor heterostructures has been proven to achieve many excellent characteristics, the photocatalytic performance can be significantly optimized in the heterostructures with piezoelectric polarization. For instance, Guo *et al*. [27] obtained an enhanced H_2 evolution rate and 4-nitrophenol degradation activity in the piezo-photocatalyst of Al/$BaTiO_3$ heterostructure. Hong *et al.* [28] achieved an extremely high piezo-photocatalytic activity in CuS/ZnO heterostructured nanowire arrays, far beyond pure ZnO. Although these results confirmed the promotion of piezoelectric polarization on photocatalytic performance, there is still great space to develop novel piezo-photocatalysts towards higher catalytic efficiency.

In this study, we designed and fabricated a piezo-photocatalyst of $BaTiO_3$/CuO heterostructure consisting of $BaTiO_3$ NWs and CuO nanoparticles (NPs). As a typical n-type ferroelectric material, $BaTiO_3$ provides driving force to separate electron–hole pairs through the built-in electric field caused by spontaneous polarization. $BaTiO_3$ NWs were chosen because the piezoelectric potential is greater than that of NPs due to the easier deformability that can effectively regulate the migration and separation of internal carriers to improve the photocatalytic performance [29]. Among the various heterogeneous photocatalysts, CuO is an excellent cocatalyst with other semiconductors due to the advantages of narrow band gap, low cost, nontoxicity, and high stability. Coupling $BaTiO_3$ with CuO to form p–n junctions is an effective way to enhance photocatalytic performance because it not only extends light absorption into the visible region but also effectively inhibits the recombination of photogenerated electron–hole pairs [30–34]. The $BaTiO_3$/CuO composites exhibit superior photocatalytic degradation ability for methyl orange (MO), much higher than that of each individual. Moreover, after being polarized by corona, the $BaTiO_3$/CuO nanocatalyst realizes a much faster degradation of dye pollutants in water upon concurrent light and mechanical stimulations.

2 Experimental

2. 1 Synthesis of $BaTiO_3$ NWs

$BaTiO_3$ NWs were prepared by a two-step hydrothermal reaction. First, 1.45 g TiO_2 was added into 10 M sodium hydroxide solution and stirred for 30 min. The solution was sealed in the Teflon-lined stainless steel autoclave and heated at 240 ℃ for 24 h to synthesize $Na_2Ti_3O_7$ NWs. The obtained $Na_2Ti_3O_7$ NWs were soaked in 0.2 M HCl with a slow stirring rate for 4 h to form $H_2Ti_3O_7$ NWs, which were converted to $BaTiO_3$ NWs by a second hydrothermal reaction. Then 0.15 g $H_2Ti_3O_7$ NWs were dispersed in 70 mL of mixed $Ba(OH)_2$ aqueous solution, and the mixed suspension was transferred to a 100 mL Teflon-lined stainless steel autoclave and kept at 210 ℃ for 85 min. After that, the obtained $BaTiO_3$ NWs were collected, washed, and then dried at 80 ℃ for 12 h.

2. 2 Synthesis of $BaTiO_3$/CuO heterostructures

$BaTiO_3$/CuO heterojunction structures were fabricated by a wet impregnation method. Typically, the synthesized $BaTiO_3$ NWs are compounded with CuO NPs in molar ratios of 1:0.2, 1:0.4, 1:0.6, 1:0.8, and 1:1 by adding

different amounts of $Cu(NO_3)_2 \cdot 3H_2O$ and dispersing in ethanol solution. After ultrasound dispersion at 30 ℃ for 30 min, the suspension was dried at 75 ℃ to obtain solid powders. Then, they were calcined in air at 300 ℃ for 2 h to synthesize $BaTiO_3$/CuO heterostructure.

2. 3 Characterization

The phase compositions of the synthesized $BaTiO_3$, CuO, and $BaTiO_3$/CuO heterostructure samples were characterized by the X-ray diffractometer (XRD; Rigaku, Japan) using the Cu Kα radiation. The morphologies of the samples were observed on a scanning electron microscope (SEM; Supra 55, Germany). The element analysis was carried out through an energy dispersive X-ray spectroscope (EDS; Supra 55, Germany). The microstructures of the nanocrystallites were observed through a field emission transmission electron microscope (FETEM; JEM-2100F, Japan) with the acceleration voltage of 200 kV. The X-ray photoelectron spectroscopy (XPS) data was obtained by using a Kratos AXIS SUPRA (UK) with monochromatic Al Kα radiation. The photocurrent was measured with an electrochemical system (CHI 700E, China) and a conventional three-electrode battery. In photocurrent measurement, the $BaTiO_3$/CuO powders were drop casted on a platinum electrode. The UV–Vis absorption spectroscopy was performed by a UV-3600 spectrophotometer equipped with an integrated sphere. The local piezoelectric response was characterized using the piezoelectric force microscope (PFM; Cypher ES, UK) with a dual alternating current resonance tracking (DART) mode. The fluorescence intensity of catalysts was recorded using the fluorescence spectroscope (FLS 980, UK). The generation of reactive species involved in the piezoelectric catalytic process was further investigated by the electron spin resonance (ESR; Bruker A300-10-12, Germany) technique.

2. 4 Catalytic activity measurement

For the catalytic degradation of MO, 0.1 g of the synthesized sample was dispersed in 100 mL of 10 $mg \cdot L^{-1}$ MO aqueous solution. After the suspension was continuously stirred in the dark for 30 min to reach an adsorption equilibrium, the ultraviolet irradiation with a 200 W xenon lamp and an ultrasonic cleaner (KQ-100DE, Kunshan Ultrasonic Instrument, China) for ultrasonic vibration were used. The reaction system was kept at ~30 ℃. At a fixed time interval of 15 min, 5 mL of the suspension was taken for sampling. After centrifugal powder removal, the concentrations of MO solutions were determined by the absorption spectra (Shimadzu UV-3600, Japan).

In addition, the cyclic stability of piezo-photocatalytic was evaluated. The MO degradation experiment was repeated by using the recycled $BaTiO_3$/CuO sample. After the completion of a piezo-photocatalytic experiment, the remaining $BaTiO_3$/CuO sample was centrifuged from the solution by a high-speed centrifuge and washed by deionized water for several times before dried at 100 ℃. Then the sample was directly polarized by the corona polarization method. Finally, the polarized $BaTiO_3$/CuO sample was employed again for the piezo-photocatalytic degradation of MO solutions.

3 Results and discussion

The crystal structures of pure $BaTiO_3$ NWs, pure CuO NPs, and $BaTiO_3$/CuO heterostructures with different molar ratios were investigated by XRD, and the results are illustrated in Fig. 1. The positions and relative intensities of all the diffraction peaks of pure $BaTiO_3$ NWs and pure CuO NPs are perfectly indexed to the tetragonal phase of $BaTiO_3$ (JCPDS Card No. 81-2203) and the monoclinic phase of CuO (JCPDS Card No. 05-0661). There is no diffractive peak of impurity for individual $BaTiO_3$ NWs and CuO NPs, indicating that they have high purity. The sharp and intense diffractive peaks of pure $BaTiO_3$ NWs and CuO NPs indicate that they have high crystallinity. For the $BaTiO_3$/CuO heterostructures, the spectra only indicate the tetragonal phase of $BaTiO_3$ NWs and the monoclinic phase of

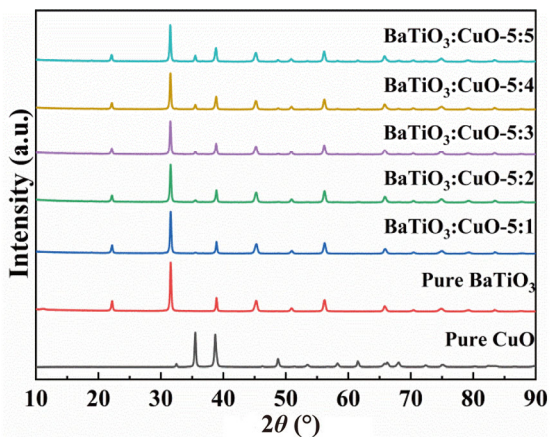

Fig. 1 XRD patterns of CuO NPs, $BaTiO_3$ NWs, and $BaTiO_3$/CuO heterostructures.

CuO NPs without any other phase. The diffractive peaks of the CuO NPs in the composite samples have very low intensities because their small particle sizes significantly broaden the Bragg reflections in comparison to pure CuO NPs.

The morphologies of $BaTiO_3$ NWs and $BaTiO_3$/CuO heterostructures are characterized by both SEM and TEM. Figure 2(a) shows that $BaTiO_3$ NWs have smooth, straight, and elongated nanostructures with a length of a few microns and a diameter of about 250 nm. When CuO NPs were deposited, a large number of small particles were observed on the surface of $BaTiO_3$ NWs, as shown in Fig. 2(b). The high-resolution TEM (HRTEM) image of the $BaTiO_3$/CuO heterojunction is shown in Figs. 2(c) and 2(d). The lattice fringes of 0.253 and 0.405 nm clearly belong to the (002) crystal plane of monoclinic CuO and the (001) crystal plane of tetragonal $BaTiO_3$, respectively. It indicates that it is the CuO NPs that adhere to the surface of $BaTiO_3$ NWs. Besides, the energy dispersive X-ray (EDX) result (Fig. 2(f)) further confirms the chemical composition of the CuO/$BaTiO_3$ heterostructures. The atom ratio of Ba to Ti is about 1:1, which is consistent with the composition of $BaTiO_3$. The elemental mapping images (Fig. 2(e)) clearly show that the Ba, Ti, and O elements uniformly distribute in the whole $BaTiO_3$ NWs, and the Cu and O elements distribute more on the surface of NWs, indicating that CuO NPs are successfully loaded on the surface of $BaTiO_3$ NWs.

In order to further verify the chemical state and the surface composition of the $BaTiO_3$/CuO heterostructures, the XPS measurement was carried out, and the survey spectrum of $BaTiO_3$/CuO is shown in Fig. 3(a). No peak of elements other than C, Ba, Ti, O, and Cu is observed, indicating that no impurity is in the sample. In Figs. 3(b) and 3(c), the peaks at 778.51, 793.79, 458.33, and 464.03 eV are attributed to Ba $3d_{5/2}$, Ba $3d_{3/2}$, Ti $2P_{3/2}$, and Ti $2P_{1/2}$, respectively, which correspond

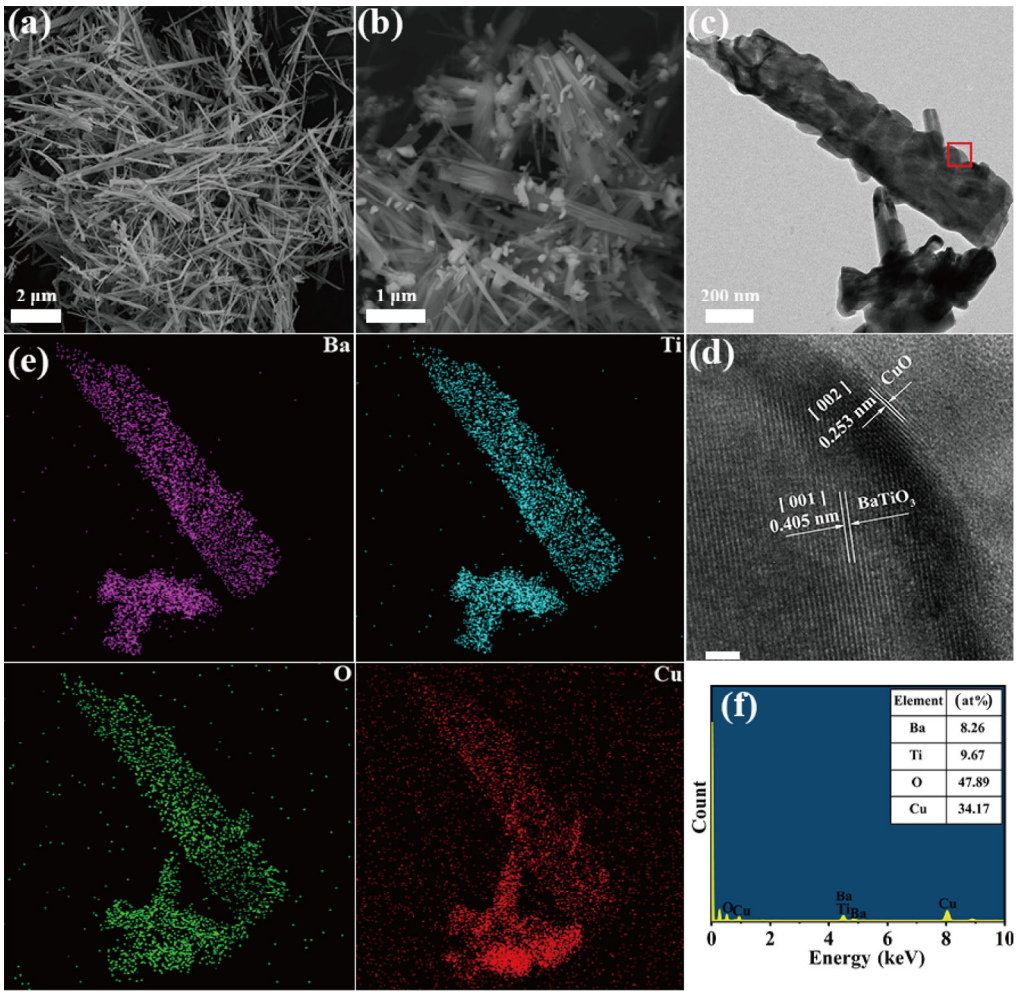

Fig. 2 SEM images of (a) $BaTiO_3$ NWs and (b) $BaTiO_3$–0.6CuO heterostructures; (c) TEM and (d) HRTEM images of $BaTiO_3$–0.6CuO; and (e) EDS spectra and (f) corresponding elemental mappings of $BaTiO_3$–0.6CuO.

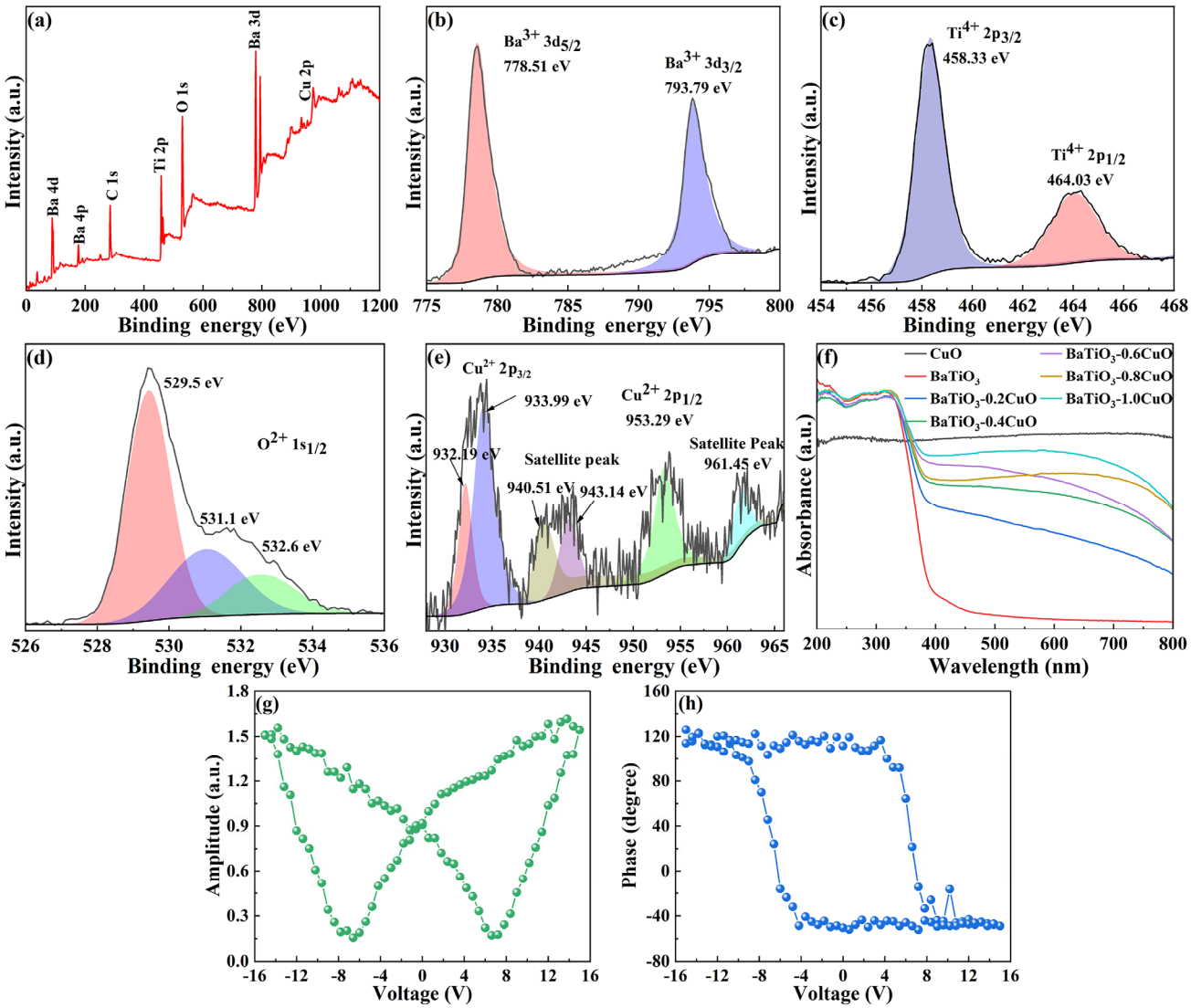

Fig. 3 XPS spectra of $BaTiO_3$–0.6CuO: (a) survey, (b) Ba 3d, (c) Ti 2p, (d) O 1s, and (e) Cu 2p; (f) UV–Vis diffuse reflectance spectra of $BaTiO_3$/CuO heterostructures; and PFM strain–voltage hysteresis loop of (g) amplitude and (h) phase for $BaTiO_3$–0.6CuO.

to the characteristic values of $BaTiO_3$. The XPS spectra of O 1s peak for $BaTiO_3$/CuO in Fig. 3(d) are fitted by three separated peaks of 529.5, 531.1, and 532.6 eV, which belong to lattice oxygen, oxygen vacancies, and chemical-absorbed oxygen, respectively. As shown in Fig. 3(e), the peaks at 933 and 953 eV confirm the oxidation state of Cu ions as 2+. The appearance of two shakeup satellite peaks, which is the feature evincing the partially filled d-orbital ($3d^9$ in Cu^{2+}), further confirms the presence of Cu^{2+}.

The optical absorption properties of the pure $BaTiO_3$ NWs, CuO NPs, and fabricated hybrid photocatalysts are characterized by UV–Vis absorption. As illustrated in Fig. 3(f), the pure $BaTiO_3$ NWs only absorb UV light with an absorption edge around 395 nm, whereas pure CuO NPs have a wide absorption range from UV to visible light. Compared to pure $BaTiO_3$ NWs, the $BaTiO_3$/CuO heterostructures exhibit significant light absorption in the visible region from 400 to 800 nm and gradually increase with increasing CuO loading, which also indicates that CuO NPs loaded on $BaTiO_3$ NWs. The piezoelectric property of $BaTiO_3$–0.6CuO heterojunctions was verified by the PFM measurement with a DART mode. Figures 3(g) and 3(h) display a typical strain–voltage hysteresis loop of ferroelectric material. The amplitude curve exhibits a typical butterfly loop in the voltage range from −15 to +15 V, and the continuous variation with the applied electric

field verifies a good local piezoelectric response. Meanwhile, the phase difference between opposite signals approaches 180°. These data suggests that the as-synthesized $BaTiO_3$–0.6CuO heterostructure shows good piezoelectric feature.

The separation and transfer of photogenerated carriers directly affect the photocurrent, which is also essential for photocatalytic reactions. Figure 4(a) represents the transient photocurrent response of $BaTiO_3$ NWs, CuO NPs, and $BaTiO_3$/CuO heterostructures with different CuO contents. All the samples display stable and reversible photocurrent responses when the light is on and off, respectively. The $BaTiO_3$–0.8CuO electrode demonstrates the largest photocurrent, which is 2.5 and 30 times higher than those of pure $BaTiO_3$ NWs and pure CuO NPs, respectively. This outcome suggests that the introduction of CuO NPs greatly enhances the charge separation efficiency of $BaTiO_3$ NWs under the irradiation of UV light. To further evaluate the photocatalytic performance of the $BaTiO_3$/CuO heterostructures, the MO degradation experiment was conducted under different UV light irradiation time. When there is no photocatalyst or only photocatalyst without UV irradiation (Figs. S1(a) and S2 in the Electronic Supplementary Material (ESM)), the MO degradation is hardly observed, which reveals that the irradiation of UV light and the adsorption of catalysis have a negligible influence on dye decomposition. In Figs. 4(b)–4(d) and Fig. S3 in the ESM, under the irradiation of UV light, the pure $BaTiO_3$ NWs exhibit a low degradation rate of MO solution, demonstrating the inherent poor photocatalytic performance of $BaTiO_3$ NWs. In contrast, the $BaTiO_3$/CuO heterostructures exhibit a significantly enhanced photocatalytic degradation of MO degradation. It is attributed to the construction of $BaTiO_3$/CuO heterostructures that provides an effective channel to facilitate the separation of electronhole pairs, which extends the lifetime of photogenerated carriers, and boosts the formation of reactive oxygen species and oxidation of MO. As shown in Fig. 4(e), the degradation rate of MO solution increases from 10% to 78% with the increase of CuO loading, and the photocatalytic efficiency exhibits saturation in the $BaTiO_3$–0.8CuO sample. When the CuO loading further increases, the photocatalytic activity turns to decrease. This is because the excess CuO covers the active sites on the $BaTiO_3$ NW surface, resulting in a decrease in

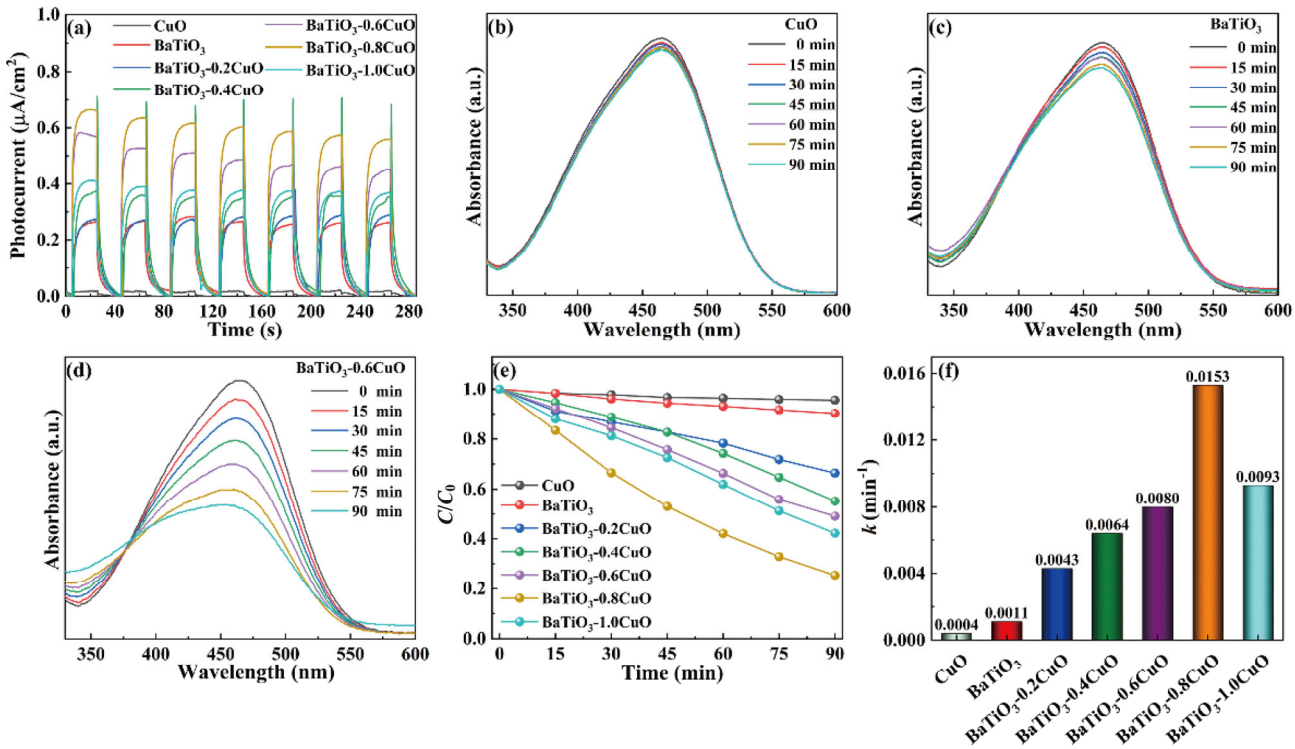

Fig. 4 (a) Transient photocurrent response of $BaTiO_3$ NWs, CuO NPs, and $BaTiO_3$–CuO heterostructures under UV irradiation. UV–Vis absorption spectra of MO solutions undergoing different UV irradiation time for (b) CuO NPs, (c) $BaTiO_3$ NWs, and (d) $BaTiO_3$–0.6CuO. (e) Comparison of photocatalytic activity of MO degradation and (f) corresponding reaction rate constant of photocatalytic.

photocatalytic activity. This result is consistent with that of the photocurrent. The catalysis reaction rate can be evaluated by a pseudo-first-order equation as follows:

$$\ln(C/C_0) = -kt \quad (1)$$

where C_0 and C are the maximum absorption peaks of MO with λ_{max} = 464 nm at 0 and t, respectively. The rate constant k of reaction is obtained from the slope of the $\ln(C_0/C)$–t curve, as shown in Fig. 4(f). The k value of the $BaTiO_3$–0.8CuO composite is calculated as 0.0153 min^{-1}, which is 13.9 and 38.2 times higher than those of pure $BaTiO_3$ NWs and pure CuO NPs, respectively.

Whereafter, the performance of the piezocatalytic degradation of MO is characterized under ultrasonic vibration. It is noted that a slight decolourisation of the MO dye solution occurs without any piezoelectric catalyst under ultrasonic activation for 90 min, which is attributed to the activation of water under ultrasound, but this is negligible for the complete degradation of dye molecules in this work (Fig. S1(b) in the ESM). In contrast, as shown in Figs. 5(a) and 5(b), after the addition of $BaTiO_3$ NWs, the decomposition ratio of MO dye is significantly enhanced. When $BaTiO_3$ NWs are laid in the MO dye solution under ultrasonic excitation, the removal efficiency of the MO dye solution reaches 69% after 90 min. It is much higher than that of the photocatalysis due to its excellent piezoelectric properties. Whereas, after the addition of CuO, there is almost no degradation for MO solutions due to the lack of piezoelectricity of CuO. These results demonstrate that the piezoelectric potential induced in the piezoelectric materials under ultrasound plays a key role in the piezocatalysis of dye degradation. When $BaTiO_3$ NWs are combined with CuO NPs, the reduction in their overall piezoelectricity will lead to an inevitable limitation in their piezocatalytic performance. As depicted in Figs. 5(c) and 5(d) and Fig. S4 in the ESM, the piezocatalytic performance of $BaTiO_3$/CuO heterostructures decreases with the increase of CuO loading.

The piezo-photocatalytic performance of the as-prepared samples was then exploited under simultaneous light illumination and ultrasonic vibration. Inspiringly, the catalytic activity of the obtained catalysts is significantly enhanced under both light and ultrasound irradiation, as shown in Fig. 6 and Fig. S5 in the ESM. As mentioned above, there are still many residual MO dye molecules over $BaTiO_3$ NWs

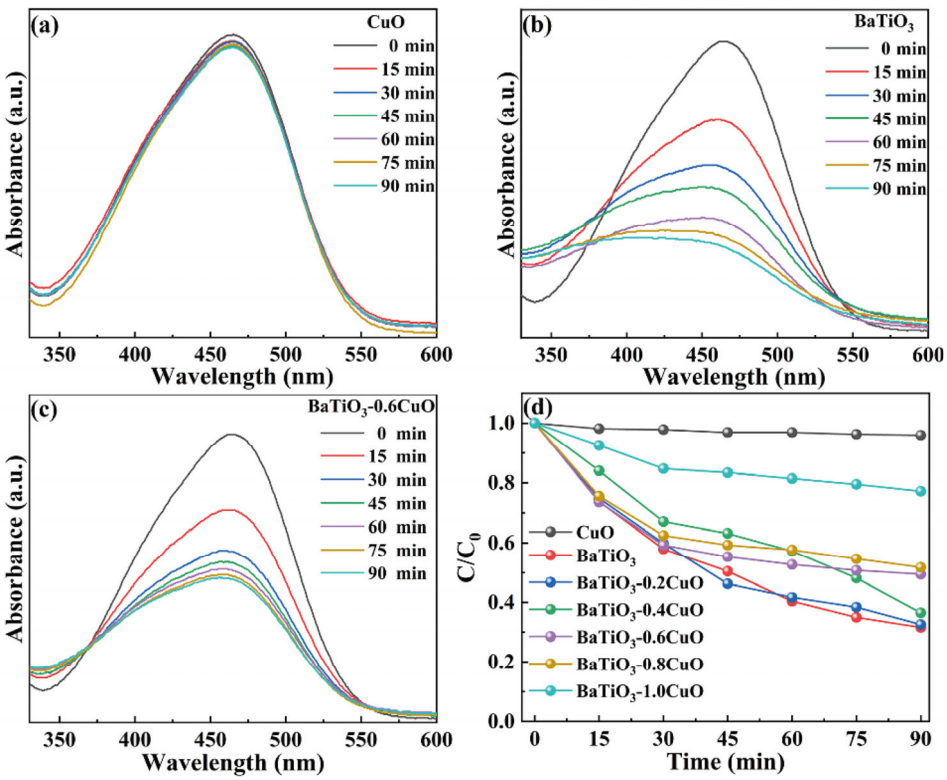

Fig. 5 UV–Vis absorption spectra of MO solutions undergoing different vibration time for (a) CuO NPs, (b) $BaTiO_3$ NWs, and (c) $BaTiO_3$–0.6CuO. (d) Comparison of piezocatalytic activity of MO degradation.

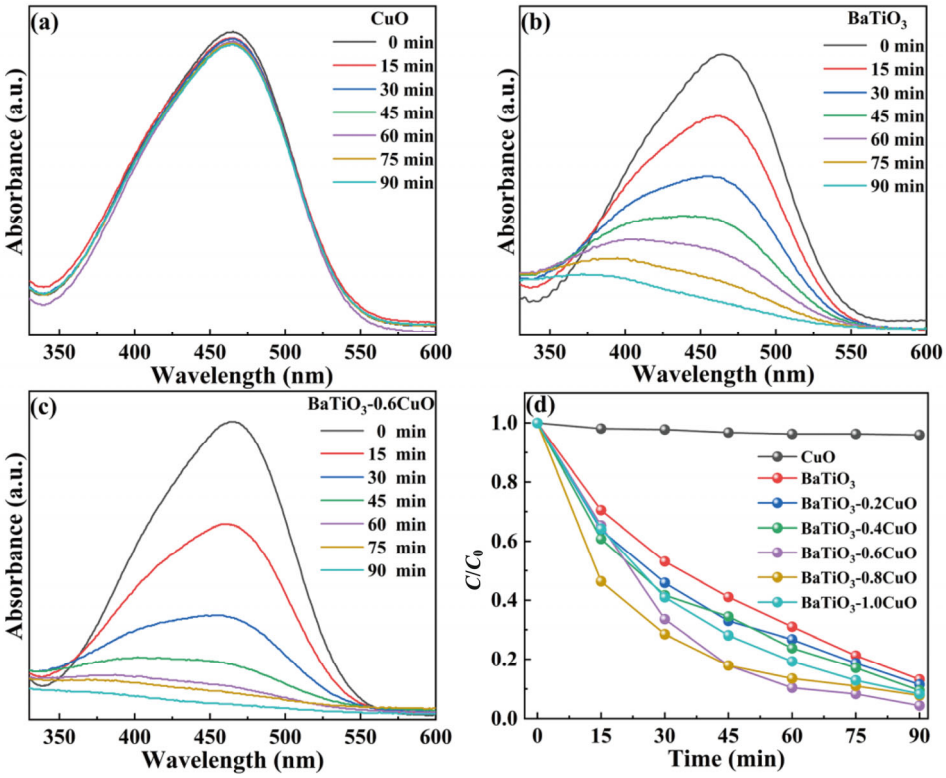

Fig. 6 UV–Vis absorption spectra of MO solutions undergoing different UV irradiation and vibration time for (a) CuO NPs, (b) $BaTiO_3$ NWs, and (c) $BaTiO_3$–0.6CuO. (d) Comparison of piezo-photocatalytic activity of MO degradation.

and $BaTiO_3$/CuO heterostructures in the photocatalytic and piezocatalytic processes for 90 min, while the degradation of MO dyes on $BaTiO_3$ NWs and $BaTiO_3$/CuO heterostructures is dramatically accelerated in the piezo-photocatalytic process. It demonstrates that the piezo-photocatalytic performances of $BaTiO_3$ NWs and $BaTiO_3$/CuO heterostructures are much higher than those of individual piezocatalysis and photocatalysis. The comparison of degradation rate constants of MO dye in the presence of $BaTiO_3$ NWs and $BaTiO_3$/CuO heterostructures under photocatalysis, piezocatalysis, and piezo-photocatalysis for 90 min is shown in Fig. 7(f). The piezo-photocatalytic reaction rates of $BaTiO_3$ NWs and $BaTiO_3$/CuO heterostructures are much greater than the sum of photocatalytic and piezocatalytic reaction rates. Moreover, the decomposition of MO dye molecules is almost complete within 90 min with a supreme degradation rate of 0.035 min^{-1} over $BaTiO_3$–0.6CuO composites, which is significantly higher than that of pure $BaTiO_3$ NWs and CuO NPs. These results imply that the synergistic effect of the heterojunction between $BaTiO_3$ NWs and CuO NPs and the internal build-in field caused by piezoelectric polarization can effectively accelerate the photoexcited electron–hole pair separation and transfer in piezo- photocatalytic reactions, resulting in the involvement of more charge carriers in photo-redox catalysis. Furthermore, when CuO NPs are excessively loaded, the piezo-photocatalytic activity drops. It is because excessive CuO NPs may (1) cover the active sites on the surface of $BaTiO_3$ NWs, which prevents the migration of charge carriers, and (2) hinder the mechanical vibration of piezoelectric material.

As a ferroelectric material, $BaTiO_3$ has multiple spontaneous polarization directions. In order to keep the energy at a low level, domains are usually formed in the $BaTiO_3$, and adjacent domains usually have different orientations. The presence of these domains with different orientations results in the electrical neutrality $BaTiO_3$ apparently and the absence of overall piezoelectricity. It needed to rearrange these domains in a uniform direction by electric field to achieve a significant improved piezoelectric property. Hence, the poling process has an impact on the piezo-photocatalytic activity. The as-prepared $BaTiO_3$/CuO samples were poled by a corona-poling method, as shown in Fig. 7(a). The catalytic performance of the polarized $BaTiO_3$ NWs is much better than that of the non-polarized sample (Fig. 7(c)), while there is no obvious change in that of CuO after polarization (Fig. 7(b)). It implies that the key role of electric polarization

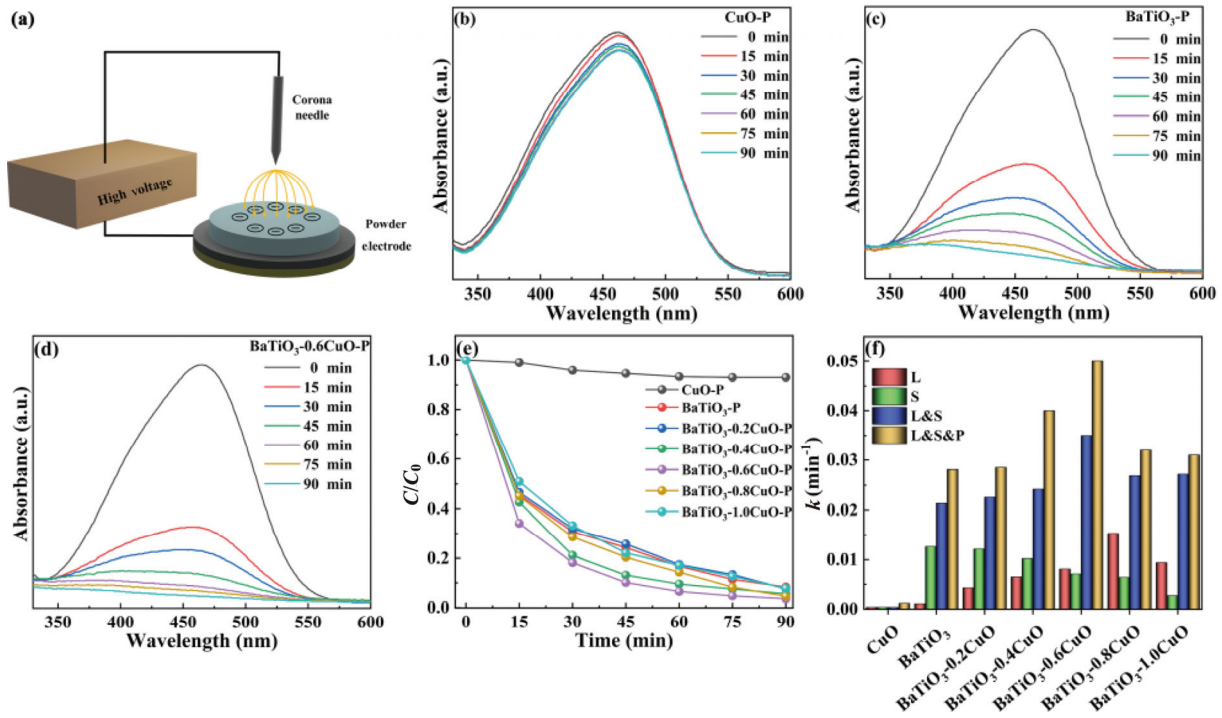

Fig. 7 (a) Illustration of the corona-poling system. UV–Vis absorption spectra of MO solutions undergoing both different UV irradiation and vibration time for (b) poled CuO NPs, (c) poled $BaTiO_3$ NWs, and (d) poled $BaTiO_3$–0.6CuO. (e) Comparison of piezo-photocatalytic activity of MO degradation with poled hybrid catalysts. (f) Comparison of degradation rate constant k for degradation of MO under various catalytic conditions (S refers to ultrasonic vibration, L refers to UV light irradiation, L & S refers to both ultrasonic and UV light, and P refers to the poled samples).

originates from the ferroelectric feature of $BaTiO_3$ NWs. From Figs. 7(d) and 7(e) and Fig. S6 in the ESM, the $BaTiO_3$–0.6CuO composite shows the best catalytic performance, achieving 90% MO degradation within 45 min. The color of MO solution exhibits an obvious change with the prolongation of reaction time, as shown in Fig. S7 in the ESM. The MO degradation for all kinds of catalysts is summarized in Fig. 7(f). By comparing the piezo-photocatalytic effect of the samples before and after poling process, it is found that the electric polarization plays an important role in enhancing the piezo-photocatalysis. Figure S8 in the ESM shows the photoluminescence spectra of unpoled $BaTiO_3$–0.6CuO and poled $BaTiO_3$–0.6CuO to evaluate the charge separation ability. The lower fluorescence emission intensity implies a higher efficiency of electron–hole pair separation. When the sample is poled, the fluorescence emission intensity is significantly reduced. It demonstrates that the polarization effectively enhances the charge separation. The rate constant k of optimal catalysis reaches 0.05 min^{-1}, which is 6.1 times that of photocatalytic rate and 7 times that of piezocatalytic rate. Moreover, the comparison of degradation efficiencies with other piezo-photocatalysts is shown in Table S1 in the ESM, where the $BaTiO_3$/CuO heterostructures exhibit excellent competitiveness [26,35–42].

From the perspective of pollutant degradation, it is necessary to determine the main reactive species in the catalytic process by adding different scavengers: disodium ethylene diamine tetra-acetate dehydrates (EDTA-2Na, hole scavengers), tert-butyl alcohol (TBA, hydroxyl radical scavengers), and benzoquinone (BQ, superoxide radical scavengers). Figure 8(a) illustrates the effects of these scavengers on the MO degradation with the polarized $BaTiO_3$–0.6CuO heterostructures as catalyst under both UV irradiation and ultrasound vibration. The decomposition rate of MO decreases to various degrees after adding scavengers, especially for superoxide radical scavengers and hole scavengers. It suggests that h^+ and O_2^- act as the main reactive species in the piezo-photocatalysis of $BaTiO_3$/CuO for MO degradation. To further identify the reactive species in the piezo-photocatalytic process, ESR experiments were carried out using DMPO and TEMP as capture reagents. As shown in Figs. S9(a) and S9(b) in the ESM, the ESR signals obtained with DMPO in aqueous

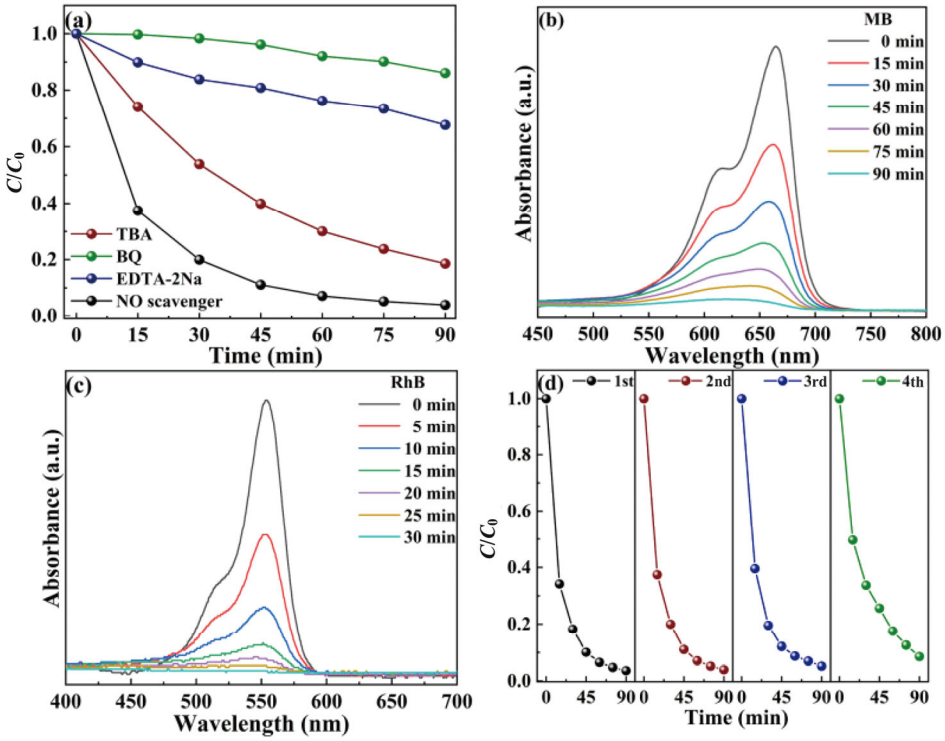

Fig. 8 (a) Piezo-photocatalytic degradation of MO by poled $BaTiO_3$–0.6CuO heterostructures in the presence of holes, electron hydroxyl radicals, and superoxide radical scavengers. UV–Vis absorption spectra of (b) methylene blue (MB) and (c) rhodamine B (RhB) aqueous solutions at different reaction time over poled $BaTiO_3$–0.6CuO heterostructures. (d) Relative intensity of the maximum absorption at 464 nm as a function of reaction time in four recycling processes.

and methanolic dispersions of $BaTiO_3$–0.6CuO correspond to hydroxyl and superoxide radicals, respectively. Apparently, no signs of free radicals were detected prior to the ultrasonic and UV illumination treatment. After 10 min of UV illumination and ultrasonic vibration, characteristic peaks for DMPO–·OH and DMPO–·O_2^- are detected. The results demonstrate that ·OH and ·O_2^- radicals are generated during piezo-photocatalysis. As displayed in Fig. S9(c) in the ESM, since TEMPO acts as a radical scavenger for h^+, the reduction of the TEMPO signal indicates that TEMPO is oxidized by h^+, revealing the generation of h^+ during piezo-photocatalysis.

In catalyst applications, the catalytic universality and cycle stability are highly desired. In Figs. 8(b) and 8(c), the piezo-photocatalysis activity of the polarized $BaTiO_3$–0.6CuO heterostructures is further examined by the degradation of other organic dyes including MB and RhB. The absorbance of different dye solutions gradually decreases with the prolongation of catalytic reaction time, which confirms a wide universality of piezo-photocatalytic activity in the polarized $BaTiO_3$–0.6CuO heterostructures. Furthermore, as shown in Fig. 8(d), after 4 times of continuous cycles, the degradation efficiency only exhibits a very slight decrease, indicating a good piezo-photocatalytic reusability. These results confirm the promising potential of $BaTiO_3$/CuO heterostructure to treat organic pollutants by the joint use of solar and mechanical energy.

A possible piezo-photocatalytic mechanism of $BaTiO_3$/CuO heterostructures is proposed and revealed in Fig. 9. First of all, the heterostructure of $BaTiO_3$/CuO has a certain contribution to photocatalytic performance. When the catalyst is illuminated, the electrons located in the valence band (VB) are excited by light to transition to the conduction band (CB), and holes are formed in the VB at the same time. Due to the difference in the energy level positions of the CB and VB of $BaTiO_3$ NWs and CuO NPs, the holes in the VB of $BaTiO_3$ NWs are transferred to the VB of CuO NPs through the interface and are accumulated. The smooth transfer of holes effectively inhibits the recombination of photo-generated electron–hole pairs. When the mechanical vibration is added, the piezoelectric effect of $BaTiO_3$ NWs produces a large number of positive and negative charges on the opposite surface of the wire, which promotes the transfer of photo-generated electrons and holes. The piezoelectric property of $BaTiO_3$ NWs is significantly improved by electrical

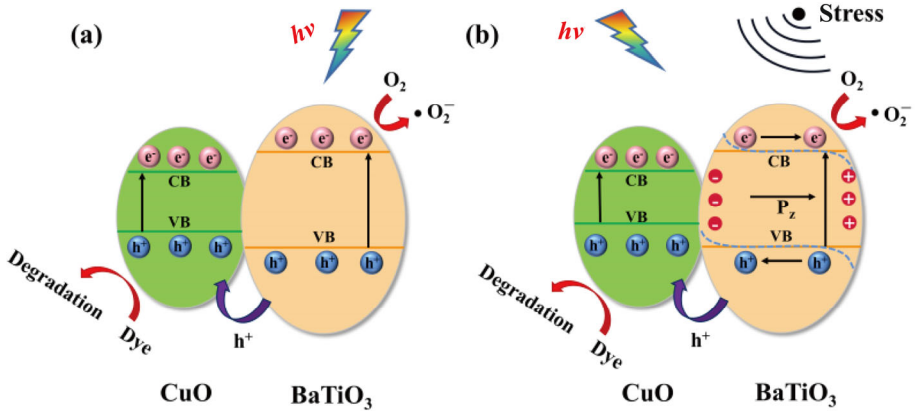

Fig. 9 (a) Proposed photocatalytic and (b) piezo-photocatalytic degradation mechanisms of $BaTiO_3$/CuO hybrid catalysts.

polarization, so do the piezocatalytic and piezo-photocatalytic properties. By comparing the piezo-photocatalytic performance before and after poling process, it is found that the piezoelectric effect plays a significant role in enhancing the piezo-photocatalytic performance.

4 Conclusions

In summary, a novel $BaTiO_3$/CuO heterojunction piezo-photocatalyst is proposed and successfully prepared. Compared with the pure $BaTiO_3$ NWs and CuO NPs, the catalytic performance of the $BaTiO_3$/CuO heterostructures to degrade organic pollutants is significantly improved under the synergistic effect of light and mechanical vibration. The optimal degradation reaction rate constant k is 0.05 min^{-1}, which is about 6.1 times and 7 times higher than that only under light and only ultrasonic vibration, respectively. The enhancement of the piezo-photocatalytic activity is attributed to the bias field generated by the piezoelectric effect of $BaTiO_3$ NWs and the built-in electric field of the $BaTiO_3$/CuO heterostructures, which effectively separates photogenerated electrons and holes. This work provides a new strategy for using the piezoelectric effect to enhance photocatalysis and shows a bright future in pollution control.

Acknowledgements

This work was supported by the Major Science and Technology Programs of Yunnan (No. 202002AB080001-1), National Natural Science Foundation of China (No. 91963114), Fundamental Research Funds for the Central Universities (No. FRF-TP-20-12B), and National Key R&D Program of China (No. 2018YFB0704301).

Electronic Supplementary Material

Supplementary material is available in the online version of this article at https://doi.org/10.1007/s40145-021-0544-4.

References

[1] Hu C, Chen F, Wang YG, *et al*. Exceptional cocatalyst-free photo-enhanced piezocatalytic hydrogen evolution of carbon nitride nanosheets from strong in-plane polarization. *Adv Mater* 2021, **33**: 2101751.

[2] Yu CY, Tan MX, Li Y, *et al*. Ultrahigh piezocatalytic capability in eco-friendly $BaTiO_3$ nanosheets promoted by 2D morphology engineering. *J Colloid Interface Sci* 2021, **596**: 288–296.

[3] Chen YX, Lan SY, Zhu MS. Construction of piezoelectric $BaTiO_3/MoS_2$ heterojunction for boosting piezo-activation of peroxymonosulfate. *Chin Chem Lett* 2021, **32**: 2052– 2056.

[4] Lan SY, Chen YX, Zeng LX, *et al*. Piezo-activation of peroxymonosulfate for benzothiazole removal in water. *J Hazard Mater* 2020, **393**: 122448.

[5] Fan KH, Yu C, Cheng ST, *et al*. Metallic Bi self-deposited BiOCl promoted piezocatalytic removal of carbamazepine. *Surf Interfaces* 2021, **26**: 101335.

[6] Wang FF, Li Q, Xu DS. Recent progress in semiconductor-based nanocomposite photocatalysts for solar-to-chemical energy conversion. *Adv Energy Mater* 2017, **7**: 1700529.

[7] Chen SS, Takata T, Domen K. Particulate photocatalysts for overall water splitting. *Nat Rev Mater* 2017, **2**: 17050.

[8] Takanabe K. Photocatalytic water splitting: Quantitative approaches toward photocatalyst by design. *ACS Catal* 2017, **7**: 8006–8022.

[9] Yu DF, Liu ZH, Zhang JM, *et al*. Enhanced catalytic performance by multi-field coupling in $KNbO_3$ nanostructures:

Piezo-photocatalytic and ferro-photoelectrochemical effects. *Nano Energy* 2019, **58**: 695–705.

[10] Pan L, Ai MH, Huang CY, *et al*. Manipulating spin polarization of titanium dioxide for efficient photocatalysis. *Nat Commun* 2020, **11**: 418.

[11] Zhang SW, Zhang BP, Li S, *et al*. Enhanced photocatalytic activity in Ag-nanoparticle-dispersed $BaTiO_3$ composite thin films: Role of charge transfer. *J Adv Ceram* 2017, **6**: 1–10.

[12] Wu ZY, Li L, Liao T, *et al*. Janus nanoarchitectures: From structural design to catalytic applications. *Nano Today* 2018, **22**: 62–82.

[13] Chen MZ, Jia YM, Li HM, *et al*. Enhanced pyrocatalysis of the pyroelectric $BiFeO_3$/g-C_3N_4 heterostructure for dye decomposition driven by cold–hot temperature alternation. *J Adv Ceram* 2021, **10**: 338–346.

[14] Hejazi S, Mohajernia S, Osuagwu B, *et al*. On the controlled loading of single platinum atoms as a co-catalyst on TiO_2 anatase for optimized photocatalytic H_2 generation. *Adv Mater* 2020, **32**: 1908505.

[15] Sadeghzadeh-Attar A. Photocatalytic degradation evaluation of N–Fe codoped aligned TiO_2 nanorods based on the effect of annealing temperature. *J Adv Ceram* 2020, **9**: 107–122.

[16] Wang ZP, Lin ZP, Shen SJ, *et al*. Advances in designing heterojunction photocatalytic materials. *Chin J Catal* 2021, **42**: 710–730.

[17] Pan L, Sun SC, Chen Y, *et al*. Advances in piezo-phototronic effect enhanced photocatalysis and photoelectrocatalysis. *Adv Energy Mater* 2020, **10**: 2000214.

[18] Xiao M, Wang ZL, Luo B, *et al*. Enhancing photocatalytic activity of tantalum nitride by rational suppression of bulk, interface and surface charge recombination. *Appl Catal B*: *Environ* 2019, **246**: 195–201.

[19] Li J, Cai LJ, Shang J, *et al*. Giant enhancement of internal electric field boosting bulk charge separation for photocatalysis. *Adv Mater* 2016, **28**: 4059–4064.

[20] Tu SC, Guo YX, Zhang YH, *et al*. Piezocatalysis and piezo-photocatalysis: Catalysts classification and modification strategy, reaction mechanism, and practical application. *Adv Funct Mater* 2020, **30**: 2005158.

[21] Yu C, Yu XX, Zheng DS, *et al*. Piezoelectric potential enhanced photocatalytic performance based on ZnO with different nanostructures. *Nanotechnology* 2021, **32**: 135703.

[22] Kumar D, Sharma S, Khare N. Piezo-phototronic and plasmonic effect coupled Ag–$NaNbO_3$ nanocomposite for enhanced photocatalytic and photoelectrochemical water splitting activity. *Renew Energy* 2021, **163**: 1569–1579.

[23] Wang ZJ, Hu TC, He HX, *et al*. Enhanced H_2 production of TiO_2/ZnO nanowires co-using solar and mechanical energy through piezo-photocatalytic effect. *ACS Sustainable Chem Eng* 2018, **6**: 10162–10172.

[24] Wang YC, Wu JM. Effect of controlled oxygen vacancy on H_2-production through the piezocatalysis and piezophototronics of ferroelectric R3C $ZnSnO_3$ nanowires. *Adv Funct Mater* 2020, **30**: 1907619.

[25] Wang MY, Zuo YP, Wang JL, *et al*. Remarkably enhanced hydrogen generation of organolead halide perovskites via piezocatalysis and photocatalysis. *Adv Energy Mater* 2019, **9**: 1901801.

[26] Hu C, Huang HW, Chen F, *et al*. Coupling piezocatalysis and photocatalysis in Bi_4NbO_8X (X = Cl, Br) polar single crystals. *Adv Funct Mater* 2020, **30**: 1908168.

[27] Guo LM, Zhong CF, Cao JQ, *et al*. Enhanced photocatalytic H_2 evolution by plasmonic and piezotronic effects based on periodic Al/$BaTiO_3$ heterostructures. *Nano Energy* 2019, **62**: 513–520.

[28] Hong DY, Zang WL, Guo X, *et al*. High piezo-photocatalytic efficiency of CuS/ZnO nanowires using both solar and mechanical energy for degrading organic dye. *ACS Appl Mater Interfaces* 2016, **8**: 21302–21314.

[29] Liu D, Jin C, Shan F, *et al*. Synthesizing $BaTiO_3$ nanostructures to explore morphological influence, kinetics, and mechanism of piezocatalytic dye degradation. *ACS Appl Mater Interfaces* 2020, **12**: 17443–17451.

[30] Reddy KH, Parida K, Satapathy PK. CuO/$PbTiO_3$: A new-fangled p–n junction designed for the efficient absorption of visible light with augmented interfacial charge transfer, photoelectrochemical and photocatalytic activities. *J Mater Chem A* 2017, **5**: 20359–20373.

[31] Tuncel D, Ökte AN. ZnO@CuO derived from Cu–BTC for efficient UV-induced photocatalytic applications. *Catal Today* 2019, **328**: 149–156.

[32] Joshi S, Canjeevaram Balasubramanyam RK, Ippolito SJ, *et al*. Straddled band aligned CuO/$BaTiO_3$ heterostructures: Role of energetics at nanointerface in improving photocatalytic and CO_2 sensing performance. *ACS Appl Nano Mater* 2018, **1**: 3375–3388.

[33] Nuengmatcha P, Porrawatkul P, Chanthai S, *et al*. Enhanced photocatalytic degradation of methylene blue using Fe_2O_3/graphene/CuO nanocomposites under visible light. *J Environ Chem Eng* 2019, **7**: 103438.

[34] Wang WZ, Wang J, Wang ZZ, *et al*. p–n junction CuO/$BiVO_4$ heterogeneous nanostructures: Synthesis and highly efficient visible-light photocatalytic performance. *Dalton Trans* 2014, **43**: 6735–6743.

[35] Zhou XF, Yan F, Wu SH, *et al*. Remarkable piezophoto coupling catalysis behavior of BiOX/$BaTiO_3$ (X = Cl, Br, $Cl_{0.166}Br_{0.834}$) piezoelectric composites. *Small* 2020, **16**: 2001573.

[36] Zhao W, Zhang Q, Wang HG, *et al*. Enhanced catalytic performance of Ag_2O/$BaTiO_3$ heterostructure microspheres by the piezo/pyro-phototronic synergistic effect. *Nano Energy* 2020, **73**: 104783.

[37] Lu LZ, Liang N, Li XF, *et al*. Highly efficient synergetic piezo/photocatalytic degradation in novel $M_{0.5}Bi_{2.5}Nb_2O_9$ (M = Li, Na, K) ferroelectric nanosheets. *Ceram Int* 2021, **47**: 8573–8583.

[38] Sharma M, Singh G, Vaish R. Dye degradation and bacterial disinfection using multicatalytic $BaZr_{0.02}Ti_{0.98}O_3$ ceramics. *J Am Ceram Soc* 2020, **103**: 4774–4784.

[39] Zhou XF, Sun QW, Zhai D, *et al*. Excellent catalytic performance of molten-salt-synthesized $Bi_{0.5}Na_{0.5}TiO_3$ nanorods by the piezo-phototronic coupling effect. *Nano Energy* 2021, **84**: 105936.

[40] Yuan J, Huang XY, Zhang LL, *et al*. Tuning piezoelectric field for optimizing the coupling effect of piezo-photocatalysis. *Appl Catal B*: *Environ* 2020, **278**: 119291.

[41] Liu YL, Wu JM. Synergistically catalytic activities of $BiFeO_3/TiO_2$ core–shell nanocomposites for degradation of organic dye molecule through piezophototronic effect. *Nano Energy* 2019, **56**: 74–81.

[42] Jia SF, Su YP, Zhang BP, *et al*. Few-layer MoS_2 nanosheet-coated $KNbO_3$ nanowire heterostructures: Piezo-photocatalytic effect enhanced hydrogen production and organic pollutant degradation. *Nanoscale* 2019, **11**: 7690–7700.